

Journal home

Advance online
publication

Current issue

Archive

Supplementary info

Careers &
Recruitment

Press releases

Supplements

Focuses

Conferences

For authors

Online submission

Permissions

For referees

Free online issue

About the journal

Contact the journal

Subscribe

Advertising

work@npg

naturereprints

About this site

For librarians

NPG Resources

Bioentrepreneur

The Nature
Biotechnology
DirectoryNature Reviews Drug
Discovery

Nature

Nature Medicine

Nature Genetics

news@nature.com

NPG Subject areas

ARTICLE

Nature Biotechnology **22**, 560 - 567 (2004)
Published online: 11 April 2004; | doi:10.1038/nbt958**Adipose-derived adult stromal cells heal critical-size mouse calvarial defects**Catherine M Cowan¹, Yun-Ying Shi¹, Oliver O Aalami¹, Yu-Fen Chou², Carina Mari³, Romy Thomas¹, Natalina Quarto¹, Christopher H Contag⁴, Benjamin Wu² & Michael T Longaker¹¹ The Department of Surgery, Stanford University School of Medicine, Stanford University, 257 Campus Drive, Stanford, California 94305, USA.² The Department of Bioengineering, University of California, Los Angeles, Los Angeles, California, USA.³ The Department of Radiology, Division of Nuclear Medicine, Stanford University School of Medicine, 300 Pasteur Drive, Stanford, California 94305, USA.⁴ The Department of Pediatrics, Stanford University School of Medicine, Stanford University, 318 Campus Drive, Stanford, California 94305, USA.Correspondence should be addressed to Michael T Longaker longaker@Stanford.edu

In adults and children over two years of age, large cranial defects do not reossify successfully, posing a substantial biomedical burden. The osteogenic potential of bone marrow stromal (BMS) cells has been documented. This study investigates the *in vivo* osteogenic capability of adipose-derived adult stromal (ADAS) cells, BMS cells, calvarial-derived osteoblasts and dura mater cells to heal critical-size mouse calvarial defects. Implanted, apatite-coated, PLGA scaffolds seeded with ADAS or BMS cells produced significant intramembranous bone formation by 2 weeks and areas of complete bony bridging by 12 weeks as shown by X-ray analysis, histology and live micromolecular imaging. The contribution of implanted cells to new bone formation was 84–99% by chromosomal detection. These data show that ADAS cells heal critical-size skeletal defects without genetic manipulation or the addition of exogenous growth factors.

Research in tissue engineering has shown the therapeutic advantages of delivering cells and growth factors in biodegradable scaffolds, which supply the necessary environmental cues to recreate a suitable niche for cellular proliferation and differentiation^{1, 2, 3, 4, 5, 6, 7, 8, 9, 10, 11}, and clinical applications have been proposed.

Calcium phosphates such as tricalcium phosphates and apatites have been reported¹² to provide such a niche for osteoblasts^{13, 14}. Biological apatite comprises a range of minerals found naturally in bone and has osteoconductive and osteophilic properties^{7, 15, 16, 17, 18}. The inherent brittleness of calcium phosphates, however, precludes their use as the

FULL TEXT

◀ Previous | Next ▶

▶ Table of contents

Download PDF

 Send to a friend

nature jobs

Lectureship

University of Reading
Reading, United
Kingdom

Various Positions

Chemistry
University of
Sunderland
Sunderland, United
Kingdom[More science jobs](#)

▼ Abstract

▼ Results

▼ Discussion

▼ Methods

▶ Figures & Tables

▼ Acknowledgments

▼ References

▶ Supplementary info

▶ Export citation

▶ Export references

▶ More articles like this

nature products

Search buyers guide:

ADVERTISEMENT

- Biotechnology
- Cancer
- Chemistry
- Clinical Medicine
- Dentistry
- Development
- Drug Discovery
- Earth Sciences
- Evolution & Ecology
- Genetics
- Immunology
- Materials Science
- Medical Research
- Microbiology
- Molecular Cell Biology
- Neuroscience
- Pharmacology
- Physics
- ▶ Browse all publications

exclusive graft material in load-bearing or large defects¹⁹. The popular polylactides (PLA) and glycolides (PGA) and other synthetic polymers such as poly lactic-co-glycolic acid (PLGA) have an established safety record in humans²⁰, but are not generally considered osteoinductive. Apatite-coated polymers combine the osteoconductive properties of bioceramics and the mechanical resilience of polymers. Scaffolds impregnated with apatite increase *in vitro* cellular attachment^{21, 22} and bone nodule formation²³, as well as *in vivo* bone formation¹⁵, providing an appropriate osteogenic environment for tissue engineering²¹.

Of the potential targets for tissue engineering and regenerative medicine, skeletal defects are perhaps most likely to meet with clinical success in the near future. Data from the US Health Cost & Utilization Project show that 12,700 craniotomies and craniectomies were performed in 2001, and procedures to correct defects associated with facial trauma numbered 20,616. The national costs for these procedures are estimated to be approximately \$549 million and \$400 million, respectively²⁴. Thus, the reconstruction of craniofacial skeletal defects represents a substantial biomedical burden.

Local application of multipotent cells has been attempted in an effort to heal critical-size or nonhealing calvarial defects; however, current systems require the addition of exogenous growth factors for sufficient and timely bone formation, usually by viral delivery^{4, 6, 10, 25}. Given current problems with gene therapy approaches, existing therapies for craniofacial defects are limited to complex reconstructive surgery, with associated morbidities. What is needed is an approach that combines scaffolds with a readily available source of osteogenic cells that do not require genetic manipulation.

The use of embryonic stem cells, which are capable of forming bone nodules²⁶, has declined because of ethical controversy; focus has shifted towards adult stem cells, especially the active multipotent precursor cells found in bone marrow^{27, 28, 29, 30, 31, 32, 33}. More recently, a second large stromal compartment found in adipose tissue has received attention and is believed to contain multipotent cells. *In vitro*, ADAS cells differentiate down osteogenic, chondrogenic, myogenic, adipogenic and even neuronal pathways^{34, 35, 36, 37, 38, 39, 40, 41, 42, 43}. Although it remains to be determined whether ADAS cells meet the definition of stem cells, they are multipotential, are available in large numbers, are easily accessible, and attach and proliferate rapidly in culture, making them an attractive cell source for tissue engineering. Moreover, ADAS cells demonstrate a substantial *in vitro* bone formation capacity^{34, 36, 37}, equal to that of bone marrow, but are much easier to culture. The *in vivo* osteogenic capability of ADAS cells placed extraskeletally has been described^{44, 45}, but their ability to heal bony defects has not yet been investigated. In this study we used ADAS cells seeded onto apatite-coated scaffolds to successfully heal critical-size skull defects in mice.

RESULTS

Uncoated versus apatite-coated PLGA scaffolds

Scaffolds seeded with juvenile calvarial-derived osteoblasts with substantial osteogenic potential⁴⁶ were implanted into critical-size (4 mm) defects. After four weeks *in vivo*, X-ray analysis showed that the osteoblasts seeded onto apatite-coated PLGA scaffolds produced high density mineralization in the area of the defect whereas osteoblasts seeded onto uncoated PLGA scaffolds did not; no mineralization was seen on coated or uncoated scaffolds without cells (Fig. 1, left column). Alizarin red staining localized bone formation to areas of mineralization (Fig. 1, center column). Although apatite-coated PLGA scaffolds absorbed some alizarin red stain in the absence of bone formation, bone-specific staining was distinguishable. H&E staining showed characteristic bone morphology only in defects implanted with apatite-coated PLGA scaffolds seeded with juvenile calvarial-derived osteoblasts (Fig. 1, right column).

bioentrepreneur
from bench to boardroom

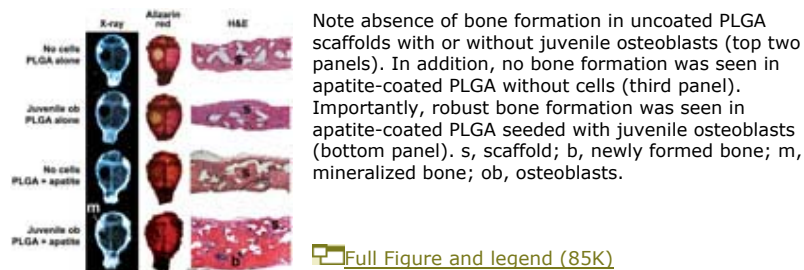
A portal
dedicated to
entrepreneurs
and **scientists**
interested in
commercializing
their research.

Content includes:

- Bio News
- New Business Advice
- Start-up Profiles
- Business Toolkit

nature publishing group 

Figure 1. X-ray, alizarin red and histological analysis of specimens at 4 weeks.



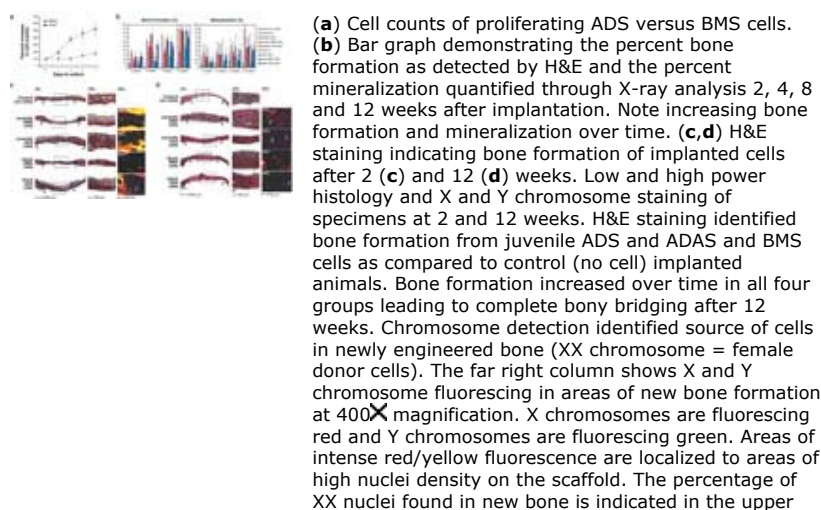
Critical-size defect determination

Defects of 0.8 mm, 2 mm, 3 mm, 4 mm and 5 mm were created in the right parietal bone of adult (2-month-old) male FVB mice, implanted with apatite-coated PLGA scaffolds without cells, and analyzed after 12 weeks of healing. Defects of 0.8 mm completely healed within the 12-week period (see [Supplementary Fig. 1](#) online) as did 0.8 mm defects that were not implanted with a scaffold (data not shown). Defects of 2 mm and larger that were implanted with apatite-coated PLGA without cells did not heal during the 12-week time period (see [Supplementary Fig. 1](#) online), nor did defects of corresponding sizes without implanted scaffolds (data not shown). These larger defects showed only minimal (<10%), unorganized bone formation as seen by X-ray analysis and H&E staining. These results identified 2 mm or larger defects as critical-size or nonhealing defects.

BMS and ADS cell culture

BMS and adipose-derived stromal (ADS) cells were harvested from juvenile (3 to 6-d-old) and adult (2 to 3-month-old) FVB mice. ADS cells showed greater attachment (data not shown) and proliferation ([Fig. 2a](#)) profiles on culture dishes than BMS cells. Freshly harvested BMS cells required 2 to 3 weeks to reach subconfluence, whereas freshly harvested ADS cells reached subconfluence in only 2–3 d (data not shown). First passage ADAS and BMS cell proliferation rates were examined by cell counting, and western blot analysis was done for proliferating cellular nuclear antigen (PCNA), a protein whose expression correlates with proliferation rate. ADS cells proliferated substantially more than BMS cells over a period of 7 d ([Fig. 2a](#)). Finally, ADAS cells produced substantial PCNA, whereas BMS cells produced almost none (data not shown). As a control, loading of total protein was examined by β -actin western blot analysis.

Figure 2. Proliferation and bone formation of ADS and BMS cells.



left corner of each frame and the presence of male XY nuclei is indicated with white arrows. Female donor cells comprised 92–99% of cells in regenerated bone. The left column shows the area of the defect taken with an original magnification of 25 \times . Black arrows indicate the osteogenic fronts. The area in the box is magnified in the center column with 200 \times magnification.

 [Full Figure and legend \(135K\)](#)

All cell types developed multiple cellular projections in three dimensions in attaching to apatite-coated PLGA scaffolds whereas those in culture dishes did not (data not shown), indicating potential differences in mechanotransduction. Additionally, no statistical differences were detected among cell groups (passages 1–3) in attachment rates to the apatite-coated PLGA scaffold (data not shown). Thus, the different seeding efficiencies of cell types were not a cause of differential *in vivo* bone formation rates.

Comparative bone formation over time

Female juvenile ADS and ADAS cells, BMS cells, calvarial-derived osteoblasts and dura mater cells were seeded onto apatite-coated PLGA scaffolds, implanted into 4 mm critical-size right parietal defects of male FVB mice, and analyzed after 2, 4, 8 and 12 weeks. Bone formation was quantified through H&E staining of calvarial sections ([Fig. 2b](#), left). In general, each group displayed increased bone formation over the 12-week time period, except for the control (no cell) implanted animals, in which there was almost no bone formation. Calvarial-derived osteoblasts, BMS cells and ADS cells all demonstrated maximal bone formation at the 12-week time point, filling 70–90% of the area of the defect.

Mineralization was quantified through X-ray analysis. All groups showed increased mineralization over time, except for the adult-derived dura mater cell group, which maintained a baseline mineralization level close to control (no cell) animals ([Fig. 2b](#), right). Importantly, by the 12-week time point, juvenile calvarial-derived osteoblasts mineralized more bone than all other groups. There were no substantial differences between ADS and BMS cell mineralization rates.

Because mineralization can be observed radiographically only several weeks after bone formation, we also investigated juvenile ADS- and ADAS- and BMS-cell bone formation through H&E staining and compared to no-cell controls. All four groups demonstrated substantial bone formation by 2 weeks, which grew to areas of complete bony bridging through the 12-week healing period, whereas no-cell controls did not ([Fig. 2c,d](#)). By 2 weeks of healing, bone formation appeared as islands within the area of the defect and was not contiguous with the bony fronts ([Fig. 2c](#)). Additionally, new bone formation was localized to the area of the scaffold adjacent to the dura mater, potentially indicating strong paracrine signaling between the underlying dura mater and the cells within the defect. Implanted versus host cell contribution to new bone was investigated through X and Y chromosome detection. At 2 weeks, new bone was determined to consist of 96–99% implanted female donor cells.

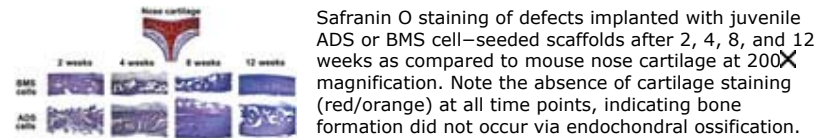
After 4 weeks of healing, new bone formation had increased in island size and number, but remained distinct from the osteogenic fronts (see [Supplementary Fig. 2](#) online). New bone, which was previously located only next to the dura mater, expanded further into the scaffold, with 85–97% of the nuclei identified as the implanted female donor cells. By 8 weeks of healing, implanted cells had formed enough bone to span most of the defect and contributed 84–99% of the new bone (see [Supplementary Fig. 2](#) online). Note the thickening of the osteogenic fronts at this time. By 12 weeks after implantation, ADS and BMS cell groups had formed complete bony bridging in areas of the defect spanning the two bony fronts ([Fig. 2d](#)). New bone was quantified to consist of 92–99% implanted female donor cells. Interestingly, at each time point, bone formation was histologically similar between ADS and BMS cells, as well as between juvenile- and adult-derived cells.

Like ADS and BMS cells, juvenile and adult calvarial-derived osteoblasts and dura mater cells formed minimal amounts of bone by 2 weeks, which increased throughout the study period (data not shown). Twelve weeks after implantation, juvenile calvarial-derived osteoblasts formed complete bony bridging, whereas adult calvarial-derived osteoblasts formed substantial bone, but did not completely bridge the defect (see [Supplementary Fig. 2](#) online). Both juvenile- and adult-derived dura mater cells formed minimal bony islands that did not span the area of the defect at 12 weeks.

Intramembranous versus endochondral bone formation

Intramembranous versus endochondral bone formation was investigated through analysis of cartilage formation. Samples implanted with juvenile ADS and BMS cells were stained with safranin O in order to identify cartilage formation. Whereas nasal cartilage showed positive staining (red/orange), both ADS and BMS cells showed an absence of cartilage staining after 2, 4, 8 and 12 weeks of healing, indicating that bone formation occurred through intramembranous ossification ([Fig. 3](#)).

Figure 3. Intramembranous versus endochondral bone formation.

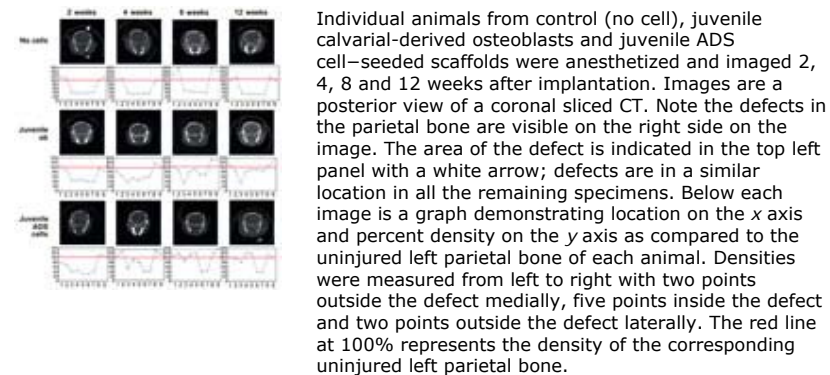


[Full Figure and legend \(43K\)](#)

Live micro-CT imaging of calvarial-derived osteoblasts and ADS cells

Increasing bone density of individual animals was examined over time. Live micro-computed tomography (CT) images were captured, and specific areas of bone formation were revisited over time in the same animal as identified by bone landmarks and defect size ([Fig. 4](#)). Bone density was measured at nine points on the right parietal bone containing the defect, from medial to lateral, including: two areas outside the defect, five areas within the defect and two more areas outside the defect. These areas were compared to the bone density of the symmetrical uninjured left parietal bone for each animal, which was set to a control density value of 100%.

Figure 4. Live micro-CT imaging.



[Full Figure and legend \(97K\)](#)

Control animals (no cells) did not show any increase in radiopacity in the

area of the defect over the 12-week time period as demonstrated by micro-CT (Fig. 4, upper row). The observed radiopacity in the area of the defect was due to the apatite coating on the scaffolds and quantified to be 25–50% of the left parietal bone radiopacity for each animal.

Juvenile calvarial-derived osteoblasts, a cell type known through histology and X-ray data to be highly osteogenic, showed baseline radiopacity at the 2-week time point; this increased over time, as seen through micro-CT imaging (Fig. 4, middle row). By 8 weeks, new bone reached 90% of the radiopacity found on the uninjured left parietal bone, and after 12 weeks, normal bone density had almost spanned the defect.

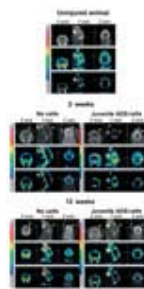
Juvenile ADS cells also showed baseline radiopacity at 2 weeks, which increased over time as seen through micro-CT imaging (Fig. 4, lower row). After only 4 weeks, much more quickly than did juvenile calvarial-derived osteoblasts, the new bone radiopacity equaled 90% of that found in the uninjured left parietal bone. By 8 weeks, new bone mineralization had exceeded the uninjured bone radiopacity by 20%. Areas of new bone did not completely mineralize the defect by 12 weeks, but remained denser than the uninjured left parietal bone.

Bone metabolic activity of ADS cells

Osteoblastic metabolic activity of immature new bone formation precedes mature bone formation and mineralization by several weeks. A bone scan measures the osteoblastic metabolic rate by reading incorporation of radiolabeled phosphorus into newly forming bone at the regenerating surface of the trabeculae. Given the substantial osteogenic potential of ADS cells based on histology, X-ray and micro-CT data, we further investigated their metabolic activity.

The metabolic activity for juvenile ADS cells was measured against control (no cell) implanted animals (Fig. 5). In uninjured animals, craniofacial areas with high physiological incorporation included cranial sutures and the mandible. Not surprisingly, these areas corresponded to growth plates and open ossification centers (Fig. 5, top panel). Metabolic increases of two- to threefold over baseline indicated the presence of inflammation, whereas increases of 10- to 15-fold indicated bone metabolism.

Figure 5. Bone metabolic activity of animals implanted with control (no cells) or ADS cell-seeded scaffolds as determined by radiolabeled MDP incorporation overlaid with micro-CT images.



For each time point, the top row displays the micro-CT scan, the middle row displays the metabolic activity, and the lower row displays the overlaid composite of metabolic activity and micro-CT scan. For all columns at each time point, the left column is the x axis, the middle column is the y axis and the right column is the z axis. For orientation, we have marked the defect with a yellow arrow for the three views of the micro-CT image. The location of the defect does not change between 2 and 12 weeks. Bone scan intensity is indicated in color on the left axis of the image with white and red indicating the highest value and black and blue indicating the lowest value.

 [Full Figure and Legend \(144K\)](#)

One day after implantation, control animals (no cells) displayed an absence of metabolic activity in the area of the defect, but high metabolic activity at the osteogenic fronts (data not shown). Similarly, animals treated with ADS cells showed minimal metabolic activity in the area of the defect, with the characteristic high metabolic activity in the osteogenic fronts. Two weeks after implantation, the metabolic activity of control animals (no cells) remained unchanged, with high metabolic activity at the osteogenic fronts

and no metabolic activity in the area of the defect. In contrast, animals treated with juvenile ADS cells showed a dramatic increase in metabolic activity in the defect as well as the osteogenic fronts (Fig. 5, middle panel). At the 8-week time point, the metabolic levels of animals with juvenile ADS cells remained elevated, whereas those of control animals (no cell) remained low (data not shown). However, by 12 weeks, both control (no cell) animals and animals implanted with juvenile ADS cells had reduced metabolic activity to equivalently low levels, indicating the return of the ADS cell-implanted animals to a resting metabolic state (Fig. 5, lower panel). Interestingly, this correlates to a time of bony bridging.

▲ [Top](#)

DISCUSSION

Current craniofacial surgery techniques use a combination of autogenous, allogeneic and prosthetic materials. Autografts are clinically limited by the donor supply and associated harvesting morbidity. Prosthetic materials avoid these issues, but their effectiveness is limited by unpredictable graft resorption, infection, structural failure and unsatisfactory aesthetic outcomes^{47, 48, 49}. Protein-based and gene-based therapies aim to deliver factors needed during endogenous wound healing. Factors, such as transforming growth factor- β , activin A, bone morphogenetic protein, fibroblast growth factor, insulin-like growth factor, growth hormone, parathyroid hormone and parathyroid hormone-related protein, and platelet rich plasma, are being investigated for their osteogenic ability^{47, 50}. The field of regenerative medicine combines various approaches, such as the cell-seeded scaffolds used in our study, to repair tissue defects. The goal of this research remains to find the most appropriate osteogenic cell type(s) and delivery method(s), which are speedy, safe and clinically relevant.

Our results provide evidence that non-genetically manipulated ADAS cells, seeded onto apatite-coated PLGA scaffolds, can regenerate bone in adult critical-size calvarial defects. The osteogenic abilities of ADAS and BMS cells were similar as judged by histology and X-ray analysis. In addition, our study refrained from the use of growth factors and from genetic manipulation of the cells, avoiding the problems of gene therapy^{4, 6, 10, 25}.

ADAS cells have several advantages over BMS cells from the perspective of clinical application. Our harvesting technique usually yields ~800 mg of subcutaneous fat tissue and 0.6 mg bone marrow per mouse. Thus, the yield of cells is much higher from fat than from bone marrow. Furthermore, the proliferation rate of ADAS cells was substantially higher than BMS cells during subsequent *in vitro* expansion. Because ADAS cells proliferate rapidly in culture, populations can readily reach the enormous cell numbers needed for clinical application. The ease of harvest, large number of cells and rapid *in vitro* expansion are attractive advantages of ADAS cells over BMS cells when contemplating clinical strategies. Moreover, the use of autogenous ADAS cells may circumvent many of the current limitations associated with bone grafts. A patient's own ADAS cells could be harvested and epigenetically expanded in culture, seeded onto apatite-coated PLGA scaffolds, and implanted into calvarial defects.

Studies have documented an interaction between juvenile dura mater and cranial osteoblasts during the bone induction processes of calvarial morphogenesis, cranial suture fusion and calvarial reossification^{51, 52, 53, 54, 55, 56}. Interestingly, the first evidence of bone formation in this study was located directly next to the dura mater, further supporting the idea of strong paracrine signaling between the underlying dura mater and overlying calvaria. With time, bone formation progressed in an endocranial to ectocranial direction into the scaffold, eventually forming a thickness comparable to the uninjured left parietal bone.

Results from several experimental systems suggest that cells from one tissue type can form other tissue types after transplantation. This could be due to the presence of multipotent or several types of adult progenitor cells in donor tissues, or alternatively, to fusion of donor and recipient cells^{57, 58, 59, 60}. In

our study, histological examination, X-ray examination and live microimaging, taken together, revealed a robust area of bony tissue regeneration. However, we cannot rule out the possibility that the regenerated bony tissue could be due to fusion of donor and recipient cells. Nevertheless, whether bone formation was due to the contribution of the multipotent cells or hybrid cells, our data demonstrate repair of critical-size bone defects and emphasize the utility of apatite-coated PLGA scaffolds seeded with ADAS or BMS cells in skeletal regenerative medicine.

▲ [Top](#)

METHODS

Cell harvest and culture conditions.

All experiments followed the protocols approved by the Animal Facilities at Stanford University. FVB mice were purchased from Charles River Laboratories. For all animals, the first day of life was considered the first day after birth. Animals were housed in light- and temperature-controlled facilities and given food and water *ad libitum*. All cell types were harvested from juvenile (3- to 6-day-old) and adult (2- to 3-month-old) female FVB mice. Calvarial osteoblasts and dura mater cells were harvested as previously described⁴⁶.

ADS cells were harvested from the subcutaneous anterior abdominal wall. Inguinal fat pads were excised, washed sequentially in serial dilutions of betadine and finely minced in PBS. Tissues were digested with 0.075% Type II collagenase (Sigma) at 37 °C for 30 min. Neutralized cells were centrifuged to separate mature adipocytes and the stromal-vascular fraction. Floating adipocytes were removed and pelleted stromal cells were passed through a 100 µm cell strainer before plating.

BMS cells were isolated from hind legs (2 femurs and 2 tibias). Hind legs were serially washed with betadine solution in PBS and all soft tissues removed. Both ends of the bone were cut and culture medium with 20% FBS was forced through the marrow cavity with a syringe. Extracted cells were pelleted and incubated in water for 3 min to lyse red blood cells. Neutralized cells were then pelleted and cultured in medium containing 20% FBS. BMS cells were maintained for 5–7 d before changing medium and subsequently changed every 2–3 d in culture medium containing 10% FBS.

All cell types were cultured in DMEM, except for osteoblasts which were cultured in α -MEM, containing 10% FBS and 100 IU/ml penicillin, and 100 IU/ml streptomycin at 37 °C in an atmosphere of 5% CO₂. Cells were grown to subconfluence and passaged by standard methods of trypsinization, except bone marrow, which was lifted from the plate with a cell scraper. Only cells of passage 1 through 3 were used for all experiments.

Scaffold preparation.

PLGA scaffolds were fabricated from 85/15 poly(lactic-co-glycolic acid) (inherent viscosity = 0.61 dL/g, Birmingham Polymers) by solvent casting and a particulate leaching process. Briefly, PLGA/chloroform solutions were mixed with 200–300 µm diameter sucrose to obtain 92% porosity (volume fraction), and compressed into thin sheets in a Teflon mold. After freeze-drying overnight, scaffolds were immersed in three changes of double-distilled (dd) H₂O to dissolve the sucrose, and gently removed from the Teflon plate with a fine-tip spatula. After particulate leaching, all scaffolds were disinfected by immersion in 50%, 60% and 70% ethanol for 30 min each, followed by three rinses of ddH₂O. All scaffolds were dried under a laminar flow hood.

After scaffold fabrication, scaffolds were coated with apatite. SBF (simulated body fluid) solution was prepared with ion concentrations that were five times that of human blood plasma. All solutions were sterile filtered through a 0.22 µm PES membrane (Nalgene). Immediately before the coating process, dried PLGA scaffolds were subjected to glow discharge, argon-plasma etching (Harrick Scientific) to improve wetting and coating uniformity. Etched PLGA scaffolds were then incubated in SBF at 37 °C inside

a water-jacketed incubator. Coated PLGA scaffolds were rinsed gently with sterile ddH₂O to wash away excess sodium chloride solution, dried in a laminar flow hood and disinfected with 70% ethanol. Integrity of the apatite coating was analyzed with a scanning electron microscope (SEM). Apatite-coated scaffolds were mounted on SEM stubs (Ted Pella) and coated with carbon to improve conductivity. The secondary electron mode was applied during SEM (FEI/Phillips XL-30) observation. Energy dispersion X-ray spectrum was obtained to confirm elemental composition of the apatite structures.

Proliferation assessment.

Subconfluent cells were seeded at 5×10^3 cells per well in a 12-well dish. The number of cells per well were counted in triplicate using a hemacytometer at days 1, 3, 5 and 7. Western blot analysis was done as previously described⁴⁶. Briefly, first passage cells were seeded in equal numbers and cultured for 48 h. Cell lysate was quantified and 30 μ g of total protein was fractionated on a 15% Tris-glycine SDS-polyacrylamide gel and transferred overnight onto an Immobilon-P transfer membrane (Millipore). Membranes were probed with the following antibodies: anti-PCNA (Santa Cruz Biotechnology) and anti- β -actin (Abcam). A horseradish peroxidase-conjugated secondary antibody specific for mouse was purchased from Amersham Biosciences. Experiments were done twice.

Cell seeding.

Cells were trypsinized or lifted off culture dishes upon subconfluence, washed and quantified. Scaffolds were cut into disks of 4.5 mm diameter and seeded with 8×10^4 cells per cm² of scaffold⁶¹. Cells in a 50- μ l volume were pipetted onto the scaffold several times. Cells were allowed to adhere for 2 h and then 100 μ l of additional culture medium was added. Twenty-four hours after seeding, cell attachment was checked by identifying nuclei. The scaffolds were incubated in 300 nM DAPI stain for 5 min and nuclei quantified with a Zeiss AxioPlan immunofluorescence microscope. Additionally, cellular morphology was investigated using immunohistochemistry techniques previously described⁴⁶ and an FITC-conjugated phalloidin antibody from Molecular Probes. Forty-eight hours after seeding, cells were implanted into animals.

***In vivo* implantation and harvesting.**

Adult male FBV mice were anesthetized with 7.5 mg/kg ketamine, 0.24 mg/kg acepromazine and 1.5 mg/kg xylazine through an intraperitoneal injection. The surgical site was cleaned with ethanol and an incision was made just off the sagittal midline to expose the right parietal bone. The pericranium was removed and 0.8, 2, 3, 4 and 5 mm defects were made in the right nonsuture-associated parietal bone using a MultiPro Dremel drill with diamond-coated trephine bits under constant irrigation. Extreme caution was taken not to disturb the underlying dura mater. Before implantation, cell-seeded scaffolds were rinsed in sterile PBS to prevent transfer of medium-derived growth factors. After placement of the scaffold into the defect, the skin was sutured closed and the animal was monitored.

Samples were harvested 2, 4, 8 and 12 weeks after surgical implantation. Calvaria were fixed in 10% formalin for 24 h at 4 °C. Representative skulls were stained with 1 mg/ml alizarin red for 12 h to view bone formation. Calvaria were X-rayed using a Faxitron X-Ray at 40 kVp for 4–8 s and then decalcified overnight with decalcifying solution (Stephens Scientific). Samples were then trimmed, processed and embedded in paraffin wax. X-ray results were quantified using Scion Image Software. Critical-size defect results were obtained from two groups of experiments with a total of 2–4 animals per defect size after 12 weeks of healing. Bone formation results were compiled from three groups of experiments. The number of animals per time point and cell type are as follows: (2 weeks) eight control, five juvenile osteoblast, eight juvenile dura mater, eight juvenile BMS, four juvenile ADS, five adult osteoblast, three adult dura mater, six adult BMS and eight ADAS; (4 weeks) seven control, four juvenile osteoblast, seven juvenile dura mater, eight juvenile BMS, six juvenile ADS, five adult osteoblast, three adult dura mater, five adult BMS and seven ADAS; (8 weeks) six control, three juvenile osteoblast, seven juvenile dura mater, five juvenile BMS, six juvenile ADS, four adult osteoblast, three adult dura mater, four adult BMS and six ADAS;

(12 weeks) six control, two juvenile osteoblast, six juvenile dura mater, seven juvenile BMS, six juvenile ADS, five adult osteoblast, three adult dura mater, five adult BMS and eight ADAS.

Quantification of mineralization.

X-ray images were used to quantify mineralization. X-ray film was scanned into the computer and analyzed using Scion Image Software. A density slice technique was used and a threshold was set when the uninjured bone was highlighted. A circle with a standardized area (slightly smaller than the area of the defect so as not to include osteogenic fronts) was placed into the defect and highlighted areas, where bone was mineralized; these areas were quantified as a function of the number of pixels in the area. Uninjured, normal bone served as a control for all measurements. Defects implanted with control (no cell) scaffolds, which formed no bone histologically, were used as a reference point for the absence of bone mineralization. Mineralized scaffold itself had a very low radiopacity and was easily distinguishable from mineralized bone.

Histology and staining.

Paraffin embedded samples were sectioned at 10 μ m thickness with a microtome (Microtom). Sections were floated in a water bath at 40 °C, placed on poly-L-lysine-coated Polysine microscope slides (Erie Scientific Company) and baked at 37 °C overnight. For hematoxylin and eosin (H&E) staining, sections were dewaxed in xylenes and rehydrated in ethanol baths. Nuclei were stained with Gill no. 2 hematoxylin stain for 8 min and eosin for 10 dips. Sections were then covered with permount and cover slipped. H&E staining was done on three samples per cell type per time point.

H&E-stained sections were used for quantification of bone formation at three standardized locations within the defect. Using Bioquant software (R&M Biometrics), we drew a line through the original defect from one edge to the other edge. We measured the length of the line as it passed through bone versus the length through scaffold for each sample.

For cartilage detection, sections were incubated in 0.02% (wt/vol) Fast Green FCF (Sigma) for 30 s, 1% (vol/vol) acetic acid for 30 s and 0.1% (wt/vol) safranin O (Sigma) for 40 min. Mouse nose cartilage was run at the same time as a positive control. Two samples per cell type per time point were stained.

X and Y chromosome detection.

Mouse X Biotin probe, Mouse Y FITC probe and the Dual Color Painting Kit were purchased from ID Labs. We dewaxed 10- μ m sections with CitriSolve (Fisher Scientific) and dehydrated them in serial ethanol washes. Sections were treated three times with 0.01% pepsin for 5 min followed by serial dehydration. Probes were hybridized according to the manufacturer's protocol overnight at 37 °C in the dark. The following morning, sections were washed, stained with DAPI nuclear stain and imaged through fluorescent detection with a Zeiss AxioPlan immunofluorescence microscope. Results were derived from four serial sections from one sample each of juvenile and adult ADS and BMS cell-seeded scaffolds at each time point. Ten to twenty images were captured between the four sections for each sample. Chromosome fluorescence was localized to nuclei through correlation with the DAPI nuclear stain. The number of male and female nuclei in each sample was quantified.

Imaging.

A small animal imaging system was used because it provides the best spatial resolution for small animals, such as mice. To study osteoblastic metabolic activity, we injected mice with 2 mCi (74 MBq) of Tc^{99m}-labeled methylene diphosphonate (MDP) (Amersham Biosciences) intravenously via the tail vein. One hour later, the mice were anesthetized via intraperitoneal injection with the same anesthetic cocktail as for implantation. We imaged mice using an A-SPECTM-micro-CT position-sensitive photomultiplier gamma camera (A-SPETTM, Gamma Medica). Whole-body planar images of the animal, together with a standard (1/100 of the injected dose in 1 ml) were obtained. We obtained selective posterior and right-lateral views of the heads using a 1 mm pin-hole collimator. Localized pin-hole Single Photon Emission

Tomography (SPET) studies (2.2 mm pixel size) of the head were also acquired in 64 X 64 scaffold, 860 steps at 60 s per step, and reconstructed, taking into account the different radius of rotation (resolution in areas with mild uptake ~500 μ m voxel size). Mirage software (Segami Corporation) was used to obtain data. Density was quantified with ImageJ software (NIH Image). Images were captured for two animals per cell type per time point.

After bone scan acquisition, a micro-CT image of the mouse calvaria was taken using the same A-SPECT machine without having to move the animal's head position. The micro-CT used an X-ray tube operating at 50 kVp and 0.75 mA. To minimize skin radiation, a 1.0mm AI filter was inserted in the beam to cut off low energy X-rays. Images were captured for 0.5 s per view for 256 views in 360° vertical rotation. The detector produced a CT image with 256 projections to reduce radiation dose. Images were captured for two to three animals per cell type per time point. The micro-SPET images were converted to a 256 X 256 scaffold and micro-CT tomographic studies were fused, allowing the achievement of simultaneous metabolic and anatomical information in every single tomogram of the scans in three different spatial axes.

Note: [Supplementary information](#) is available on the Nature Biotechnology website.

▲ [Top](#)

Received 11 September 2003; Accepted 4 February 2004; Published online: 11 April 2004.

REFERENCES

1. Krebsbach, P.H. *et al.* Bone formation *in vivo*: comparison of osteogenesis by transplanted mouse and human marrow stromal fibroblasts. *Transplantation* **63**, 1059–1069 (1997). | [PubMed](#) | [ChemPort](#) |
2. Krebsbach, P.H., Mankani, M.H., Satomura, K., Kuznetsov, S.A. & Robey, P.G. Repair of craniotomy defects using bone marrow stromal cells. *Transplantation* **66**, 1272–1278 (1998). | [PubMed](#) | [ChemPort](#) |
3. Mendes, S.C. *et al.* Bone tissue-engineered implants using human bone marrow stromal cells: effect of culture conditions and donor age. *Tissue Eng.* **8**, 911–920 (2002). | [Article](#) | [PubMed](#) | [ChemPort](#) |
4. Peng, H. *et al.* Synergistic enhancement of bone formation and healing by stem cell-expressed VEGF and bone morphogenetic protein-4. *J. Clin. Invest.* **110**, 751–759 (2002). | [Article](#) | [PubMed](#) | [ChemPort](#) |
5. Vacanti, J.P., Langer, R., Upton, J. & Marler, J.J. Transplantation of cells in matrices for tissue regeneration. *Adv. Drug Deliv. Rev.* **33**, 165–182 (1998). | [Article](#) | [PubMed](#) |
6. Wright, V. *et al.* BMP4-expressing muscle-derived stem cells differentiate into osteogenic lineage and improve bone healing in immunocompetent mice. *Mol. Ther.* **6**, 169–178 (2002). | [Article](#) | [PubMed](#) | [ChemPort](#) |
7. Durham, S.R., McComb, J.G. & Levy, M.L. Correction of large (>25 cm²) cranial defects with "reinforced" hydroxyapatite cement: technique and complications. *Neurosurgery* **52**, 842–845; discussion 845 (2003). | [PubMed](#) |
8. Harris, S.E. *et al.* Effects of transforming growth factor beta on bone nodule formation and expression of bone morphogenetic protein 2, osteocalcin, osteopontin, alkaline phosphatase, and type I collagen mRNA in long-term cultures of fetal rat calvarial osteoblasts. *J. Bone Miner. Res.* **9**, 855–863 (1994). | [PubMed](#) | [ChemPort](#) |
9. Dong, J. *et al.* *In vivo* evaluation of a novel porous hydroxyapatite to sustain osteogenesis of transplanted bone marrow-derived osteoblastic cells. *J. Biomed. Mater. Res.* **57**, 208–216 (2001). | [Article](#) | [PubMed](#) | [ChemPort](#) |
10. Lee, J.Y. *et al.* Effect of bone morphogenetic protein-2-expressing muscle-derived cells on healing of critical-sized bone defects in mice. *J. Bone Joint Surg. Am.* **83-A**, 1032–1039 (2001). | [PubMed](#) | [ChemPort](#) |

11. Shea, L.D., Wang, D., Franceschi, R.T. & Mooney, D.J. Engineered bone development from a pre-osteoblast cell line on three-dimensional scaffolds. *Tissue Eng.* **6**, 605–617 (2000). | [Article](#) | [PubMed](#) | [ChemPort](#) |
12. Muller-Mai, C.M., Stupp, S.I., Voigt, C. & Gross, U. Nanoapatite and organoapatite implants in bone: histology and ultrastructure of the interface. *J. Biomed. Mater. Res.* **29**, 9–18 (1995). | [PubMed](#) | [ChemPort](#) |
13. Reddi, A. Bioceramics, cells and signals in tissue engineering. *Bioceramics, Proceedings of the International Symposium on Ceramics in Medicine* **11**, 9–11 (1998). | [ChemPort](#) |
14. Hench, L.L. Bioceramics. *J. Am. Ceramic Soc.* **81**, 1705–1728 (1998). | [ChemPort](#) |
15. Bourgeois, B. *et al.* Calcium-deficient apatite: a first *in vivo* study concerning bone ingrowth. *J. Biomed. Mater. Res.* **65A**, 402–408 (2003). | [Article](#) | [ChemPort](#) |
16. Neo, M. *et al.* A comparative study of ultrastructures of the interfaces between four kinds of surface-active ceramic and bone. *J. Biomed. Mater. Res.* **26**, 1419–1432 (1992). | [Article](#) | [PubMed](#) | [ChemPort](#) |
17. van Blitterswijk, C.A., Hesselink, S.C., Grote, J.J., Koerten, H.K. & de Groot, K. The biocompatibility of hydroxyapatite ceramic: a study of retrieved human middle ear implants. *J. Biomed. Mater. Res.* **24**, 433–453 (1990). | [Article](#) | [PubMed](#) | [ChemPort](#) |
18. Le Huec, J.C., Schaefferbeke, T., Clement, D., Faber, J. & Le Rebellier, A. Influence of porosity on the mechanical resistance of hydroxyapatite ceramics under compressive stress. *Biomaterials* **16**, 113–118 (1995). | [Article](#) | [PubMed](#) | [ChemPort](#) |
19. Sarkar, B.K. Fatigue of brittle materials—a critical appraisal. *Bull. Mater. Sci.* **18**, 755–772 (1995). | [ChemPort](#) |
20. Frazza, E.J. & Schmitt, E.E. A new absorbable suture. *J. Biomed. Mater. Res.* **5**, 43–58 (1971). | [Article](#) | [PubMed](#) | [ChemPort](#) |
21. Rosa, A.L., Beloti, M.M., Van Noort, R., Hatton, P.V. & Devlin, A.J. Surface topography of hydroxyapatite affects ROS17/2.8 cells response. *Pesqui. Odontol. Bras.* **16**, 209–215 (2002). | [PubMed](#) |
22. Okumura, A. *et al.* Substrate affects the initial attachment and subsequent behavior of human osteoblastic cells (Saos-2). *Biomaterials* **22**, 2263–2271 (2001). | [Article](#) | [PubMed](#) | [ChemPort](#) |
23. Zhao, F. *et al.* [Tissue engineering study on chitosan-gelatin/hydroxyapatite composite scaffolds—osteoblasts culture]. *Zhongguo Xiu Fu Chong Jian Wai Ke Za Zhi* **16**, 130–133 (2002).
24. Steiner, C., Elixhauser, A. & Schnaier, J. The healthcare cost and utilization project: an overview. *Eff. Clin. Pract.* **5**, 143–151 (2002). | [PubMed](#) |
25. Hong, L. *et al.* Bone regeneration at rabbit skull defects treated with transforming growth factor-beta1 incorporated into hydrogels with different levels of biodegradability. *J. Neurosurg.* **92**, 315–325. (2000). | [PubMed](#) | [ChemPort](#) |
26. Buttery, L.D. *et al.* Differentiation of osteoblasts and *in vitro* bone formation from murine embryonic stem cells. *Tissue Eng.* **7**, 89–99 (2001). | [Article](#) | [PubMed](#) | [ChemPort](#) |
27. Gundle, R., Joyner, C.J. & Triffitt, J.T. Human bone tissue formation in diffusion chamber culture *in vivo* by bone-derived cells and marrow stromal fibroblastic cells. *Bone* **16**, 597–601 (1995). | [Article](#) | [PubMed](#) | [ChemPort](#) |
28. Haynesworth, S.E., Goshima, J., Goldberg, V.M. & Caplan, A.I. Characterization of cells with osteogenic potential from human marrow. *Bone* **13**, 81–88 (1992). | [Article](#) | [PubMed](#) | [ChemPort](#) |
29. Johnstone, B., Hering, T.M., Caplan, A.I., Goldberg, V.M. & Yoo, J.U. *In vitro* chondrogenesis of bone marrow-derived mesenchymal progenitor cells. *Exp. Cell. Res.* **238**, 265–272 (1998). | [Article](#) | [PubMed](#) | [ChemPort](#) |
30. Wakitani, S., Saito, T. & Caplan, A.I. Myogenic cells derived from rat bone marrow mesenchymal stem cells exposed to 5-azacytidine. *Muscle Nerve* **18**, 1417–1426 (1995). | [Article](#) | [PubMed](#) | [ChemPort](#) |
31. Jaiswal, N., Haynesworth, S.E., Caplan, A.I. & Bruder, S.P. Osteogenic differentiation of purified, culture-expanded human mesenchymal stem cells *in vitro*. *J. Cell Biochem.* **64**, 295–312 (1997). | [Article](#) | [PubMed](#) | [ChemPort](#) |
32. Toquet, J. *et al.* Osteogenic potential *in vitro* of human bone marrow

- cells cultured on macroporous biphasic calcium phosphate ceramic. *J. Biomed. Mater. Res.* **44**, 98–108 (1999). | [PubMed](#) | [ChemPort](#) |
33. Im, G.I., Kim, D.Y., Shin, J.H., Hyun, C.W. & Cho, W.H. Repair of cartilage defect in the rabbit with cultured mesenchymal stem cells from bone marrow. *J. Bone Joint Surg. Br.* **83**, 289–294 (2001). | [Article](#) | [PubMed](#) | [ChemPort](#) |
34. Halvorsen, Y.D. *et al.* Extracellular matrix mineralization and osteoblast gene expression by human adipose tissue-derived stromal cells. *Tissue Eng.* **7**, 729–741 (2001). | [Article](#) | [PubMed](#) | [ChemPort](#) |
35. Tholpady, S.S., Katz, A.J. & Ogle, R.C. Mesenchymal stem cells from rat visceral fat exhibit multipotential differentiation *in vitro*. *Anat. Rec.* **272A**, 398–402 (2003). | [Article](#) |
36. Zuk, P.A. *et al.* Multilineage cells from human adipose tissue: implications for cell-based therapies. *Tissue Eng.* **7**, 211–228 (2001). | [Article](#) | [PubMed](#) | [ChemPort](#) |
37. Zuk, P.A. *et al.* Human adipose tissue is a source of multipotent stem cells. *Mol. Biol. Cell* **13**, 4279–4295 (2002). | [Article](#) | [PubMed](#) | [ChemPort](#) |
38. Mizuno, H. *et al.* Myogenic differentiation by human processed lipoaspirate cells. *Plast. Reconstr. Surg.* **109**, 199–209 (2002). | [PubMed](#) |
39. Ashjian, P.H. *et al.* *In vitro* differentiation of human processed lipoaspirate cells into early neural progenitors. *Plast. Reconstr. Surg.* **111**, 1922–1931 (2003). | [PubMed](#) |
40. Wickham, M.Q., Erickson, G.R., Gimble, J.M., Vail, T.P. & Guilak, F. Multipotent stromal cells derived from the infrapatellar fat pad of the knee. *Clin. Orthop.* **412**, 196–212 (2003). | [PubMed](#) |
41. Halvorsen, Y.D. *et al.* Thiazolidinediones and glucocorticoids synergistically induce differentiation of human adipose tissue stromal cells: biochemical, cellular, and molecular analysis. *Metabolism* **50**, 407–413 (2001). | [Article](#) | [PubMed](#) | [ChemPort](#) |
42. Erickson, G.R. *et al.* Chondrogenic potential of adipose tissue-derived stromal cells *in vitro* and *in vivo*. *Biochem. Biophys. Res. Commun.* **290**, 763–769 (2002). | [Article](#) | [PubMed](#) | [ChemPort](#) |
43. Safford, K.M. *et al.* Neurogenic differentiation of murine and human adipose-derived stromal cells. *Biochem. Biophys. Res. Commun.* **294**, 371–379 (2002). | [Article](#) | [PubMed](#) | [ChemPort](#) |
44. Dragoo, J.L. *et al.* Bone induction by BMP-2 transduced stem cells derived from human fat. *J. Orthop. Res.* **21**, 622–629 (2003). | [Article](#) | [PubMed](#) | [ChemPort](#) |
45. Lee, J.A. *et al.* Biological alchemy: engineering bone and fat from fat-derived stem cells. *Ann. Plast. Surg.* **50**, 610–617 (2003). | [PubMed](#) |
46. Cowan, C.M., Quarto, N., Warren, S.M., Salim, A. & Longaker, M.T. Age-related changes in the biomolecular mechanisms of calvarial osteoblast biology affect FGF-2 signaling and osteogenesis. *J. Biol. Chem.* **278**, 32005–32013 (2003). | [Article](#) | [PubMed](#) | [ChemPort](#) |
47. Fong, K.D. *et al.* New strategies for craniofacial repair and replacement: a brief review. *J. Craniofac. Surg.* **14**, 333–339 (2003). | [PubMed](#) |
48. Mulliken, J.B. & Glowacki, J. Induced osteogenesis for repair and construction in the craniofacial region. *Plast. Reconstr. Surg.* **65**, 553–560 (1980). | [PubMed](#) | [ChemPort](#) |
49. Bostrom, R. & Mikos, A. (eds.) *Tissue Engineering of Bone*, vol. **1** (Birkhauser, Boston, 1997).
50. Lieberman, J.R., Daluiski, A. & Einhorn, T.A. The role of growth factors in the repair of bone. Biology and clinical applications. *J. Bone Joint Surg. Am.* **84-A**, 1032–1044 (2002). | [PubMed](#) |
51. Bradley, J.P. *et al.* Studies in cranial suture biology: *in vitro* cranial suture fusion. *Cleft Palate Craniofac. J.* **33**, 150–156 (1996). | [PubMed](#) | [ChemPort](#) |
52. Bradley, J.P., Levine, J.P., McCarthy, J.G. & Longaker, M.T. Studies in cranial suture biology: regional dura mater determines *in vitro* cranial suture fusion. *Plast. Reconstr. Surg.* **100**, 1091–1099 (1997). | [PubMed](#) | [ChemPort](#) |
53. Opperman, L.A., Passarelli, R.W., Morgan, E.P., Reintjes, M. & Ogle, R.C. Cranial sutures require tissue interactions with dura mater to resist osseous obliteration *in vitro*. *J. Bone Miner. Res.* **10**, 1978–1987 (1995). | [PubMed](#) | [ChemPort](#) |
54. Opperman, L.A. *et al.* Dura mater secretes soluble heparin-binding

- factors required for cranial suture morphogenesis. *In vitro cell dev. biol.* **32**, 150–158 (1996).
55. Mehrara, B.J. *et al.* Basic fibroblast growth factor and transforming growth factor beta-1 expression in the developing dura mater correlates with calvarial bone formation. *Plast. Reconstr. Surg.* **104**, 435–444 (1999). | [PubMed](#) | [ChemPort](#) |
 56. Greenwald, J.A. *et al.* Regional differentiation of cranial suture-associated dura mater *in vivo* and *in vitro*: implications for suture fusion and patency. *J. Bone Miner. Res.* **15**, 2413–2430 (2000). | [PubMed](#) | [ChemPort](#) |
 57. Jiang, Y. *et al.* Pluripotency of mesenchymal stem cells derived from adult marrow. *Nature* **418**, 41–49 (2002). | [Article](#) | [PubMed](#) | [ChemPort](#) |
 58. Medvinsky, A. & Smith, A. Stem cells: Fusion brings down barriers. *Nature* **422**, 823–825 (2003). | [Article](#) | [PubMed](#) | [ChemPort](#) |
 59. Wang, X. *et al.* Cell fusion is the principal source of bone-marrow-derived hepatocytes. *Nature* **422**, 897–901 (2003). | [Article](#) | [PubMed](#) | [ChemPort](#) |
 60. Vassilopoulos, G., Wang, P.R. & Russell, D.W. Transplanted bone marrow regenerates liver by cell fusion. *Nature* **422**, 901–904 (2003). | [Article](#) | [PubMed](#) | [ChemPort](#) |
 61. Wiedmann-Al-Ahmad, M., Gutwald, R., Lauer, G., Hubner, U. & Schmelzeisen, R. How to optimize seeding and culturing of human osteoblast-like cells on various biomaterials. *Biomaterials* **23**, 3319–3328 (2002). | [Article](#) | [PubMed](#) | [ChemPort](#) |

▲ [Top](#)

ACKNOWLEDGMENTS

This work has been supported by a grant from the National Institutes of Health (R01DE-14526) and the Oak foundation to M.T.L. The authors would like to thank Randall P. Nacamuli for his scientific and editorial assistance. We also acknowledge Koji Iwata and Michael Goris for their assistance with small animal imaging.

Competing interests statement: The authors declare that they have no competing financial interests.

nature
biotechnology

ISSN: 1087-0156
EISSN: 1546-1696

[Journal home](#) | [Advance online publication](#) | [Current issue](#) | [Archive](#) | [Press releases](#) | [Supplements](#) | [Focuses](#) | [Conferences](#) | [For authors](#) | [Online submission](#) | [Permissions](#) | [For referees](#) | [Free online issue](#) | [About the journal](#) | [Contact the journal](#) | [Subscribe](#) | [Advertising](#) | [work@npg](#) | [naturereprints](#) | [About this site](#) | [For librarians](#)



©2004 Nature Publishing Group | [Privacy policy](#)